






# Selective electroreduction of CO<sub>2</sub> to acetone by single copper atoms anchored on N-doped porous carbon

Kun Zhao<sup>1,5</sup>, Xiaowa Nie<sup>2,3,5</sup>, Haozhi Wang<sup>2</sup>, Shuo Chen<sup>1</sup>, Xie Quan<sup>1</sup> <sup>✉</sup>, Hongtao Yu<sup>1</sup>, Wonyong Choi<sup>4</sup> , Guanghui Zhang<sup>2</sup> , Bupmo Kim<sup>4</sup>  & Jingguang G. Chen<sup>3</sup> <sup>✉</sup>

Efficient electroreduction of CO<sub>2</sub> to multi-carbon products is a challenging reaction because of the high energy barriers for CO<sub>2</sub> activation and C–C coupling, which can be tuned by designing the metal centers and coordination environments of catalysts. Here, we design single atom copper encapsulated on N-doped porous carbon (Cu-SA/NPC) catalysts for reducing CO<sub>2</sub> to multi-carbon products. Acetone is identified as the major product with a Faradaic efficiency of 36.7% and a production rate of 336.1 μg h<sup>-1</sup>. Density functional theory (DFT) calculations reveal that the coordination of Cu with four pyrrole-N atoms is the main active site and reduces the reaction free energies required for CO<sub>2</sub> activation and C–C coupling. The energetically favorable pathways for CH<sub>3</sub>COCH<sub>3</sub> production from CO<sub>2</sub> reduction are proposed and the origin of selective acetone formation on Cu-SA/NPC is clarified. This work provides insight into the rational design of efficient electrocatalysts for reducing CO<sub>2</sub> to multi-carbon products.

<sup>1</sup>Key Laboratory of Industrial Ecology and Environmental Engineering (Ministry of Education, China), School of Environmental Science and Technology, Dalian University of Technology, Dalian 116024, PR China. <sup>2</sup>State Key Laboratory of Fine Chemicals, PSU-DUT Joint Center for Energy Research, School of Chemical Engineering, Dalian University of Technology, Dalian 116024, PR China. <sup>3</sup>Department of Chemical Engineering, Columbia University, New York, NY 10027, USA. <sup>4</sup>Division of Environmental Science and Engineering, Pohang University of Science and Technology, Pohang 37673, Republic of Korea. <sup>5</sup>These authors contributed equally: Kun Zhao, Xiaowa Nie. ✉email: [quanxie@dlut.edu.cn](mailto:quanxie@dlut.edu.cn); [jgchen@columbia.edu](mailto:jgchen@columbia.edu)

Electrochemical reduction of CO<sub>2</sub> to value-added chemicals and fuels offers a promising approach for solving issues related to energy crisis and global warming<sup>1–5</sup>. CO<sub>2</sub> can be converted to C<sub>1</sub>, C<sub>2</sub>, or C<sub>2+</sub> products via different proton- and electron-transfer steps and different CO<sub>2</sub> reduction pathways. Converting CO<sub>2</sub> to multi-carbon (C<sub>2</sub> and C<sub>2+</sub>) products is more desirable due to their higher value and higher energy density<sup>6–9</sup>.

Recently, numerous electrocatalysts have been designed for CO<sub>2</sub> reduction, such as metals, metal oxides, and carbon-based materials<sup>10–14</sup>. Among these catalysts, copper (Cu) owns the ability to generate multi-carbon products from CO<sub>2</sub> reduction. This may be related to the optimal binding energy of CO intermediate on Cu, leading to the further reduction of CO intermediate and achieving the C–C coupling<sup>12,15–17</sup>. Although Cu-based catalysts can reduce CO<sub>2</sub> to C<sub>2</sub> products, it still suffers from high barriers for CO<sub>2</sub> activation and C–C coupling, resulting in large overpotentials for C<sub>2</sub> product formation<sup>18–21</sup>. Moreover, efficient reduction of CO<sub>2</sub> to C<sub>2+</sub> products, such as C<sub>3</sub> oxygenates, on Cu-based electrocatalysts are rarely reported.

Single atom catalysts (SAC) with atomically distributed active metal centers have been demonstrated to possess enhanced activity and tunable selectivity toward CO<sub>2</sub> reduction due to its maximum atom utilization efficiency, unique electronic structure, and unsaturated coordination environment of metal centers<sup>22–24</sup>. As reported previously, partially oxidized single atom cobalt can electrochemically reduce CO<sub>2</sub> to HCOOH with a Faradaic efficiency of ~90%<sup>25</sup>. Isolated Ni centers in N- and S-doped graphene exhibit high activity toward CO production with a TOF value of 14,800 h<sup>-1</sup> and a maximum Faradaic efficiency of 97% at -0.5 V<sup>26</sup>. Single Fe(II) sites on N-doped carbon are active for reducing CO<sub>2</sub> to CH<sub>3</sub>COOH<sup>27</sup>. These results have clearly demonstrated the potential in using single atom materials as active and selective electrocatalysts for CO<sub>2</sub> reduction.

In this work, the atomically distributed Cu is anchored on N-doped porous carbon (Cu-SA/NPC) and is evaluated for CO<sub>2</sub> electrochemical reduction. The Cu-SA/NPC reduces CO<sub>2</sub> to acetic acid, ethanol, and acetone products at a low overpotential, with acetone being the major product. The effects of Cu distribution and local coordination environment of SAC on CO<sub>2</sub> reduction are investigated. The active sites of Cu-SA/NPC and mechanisms of CO<sub>2</sub> activation, C–C coupling, and CH<sub>3</sub>COCH<sub>3</sub> formation from CO<sub>2</sub> reduction are elucidated by combined experimental and density functional theory (DFT) studies.

## Results

**Characterization of Cu-SA/NPC.** The Cu-SA/NPC was synthesized by a continuous process including hydrothermal synthesis of Cu-doped ZIF-8 and subsequent carbonization of the precursor at 1000 °C under N<sub>2</sub> atmosphere. The elemental composition of obtained catalysts was characterized by XPS measurement. The NPC only showed the signal of C, N, and O elements (Supplementary Fig. 1), while the Cu-SA/NPC exhibited a small peak of Cu, indicating that Cu was successfully incorporated in the prepared material. The Cu content was determined to be about 0.59 wt% by inductively coupled plasma atomic emission spectroscopy (ICP-AES) (Supplementary Table 1). The XRD patterns of Cu-SA/NPC showed two broad diffraction peaks located at 23° and 44°, corresponding to the (002) and (101) plane of carbon, respectively (Supplementary Fig. 2). No Cu-related crystal phases were observed, which might be caused by the low loading amount of Cu species.

As shown in the scanning electron microscope (SEM) and transmission electron microscope (TEM) images, Cu-SA/NPC retained the rhombic dodecahedral morphology of the pristine ZIF precursor (Fig. 1 and Supplementary Fig. 3), while exhibiting

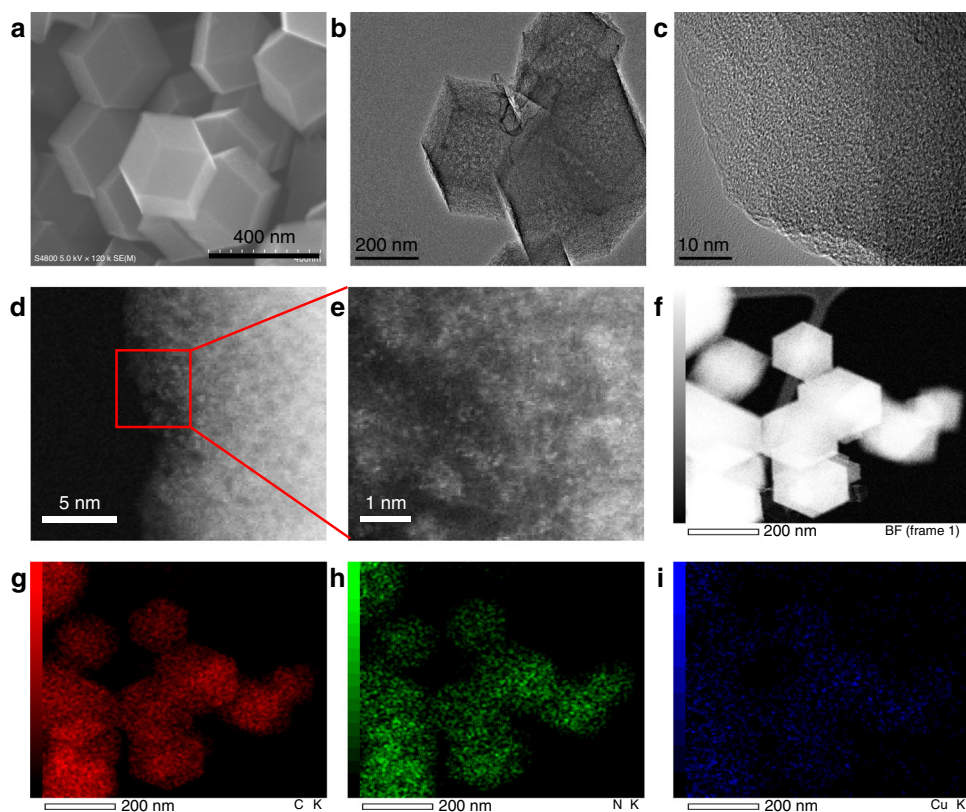


**Fig. 1** Morphological characterization of Cu-SA/NPC. **a** SEM. **b**, **c** TEM. **d**, **e** HAADF-STEM images and enlarged images. **f–i** EDS images of Cu-SA/NPC by HAADF-STEM.

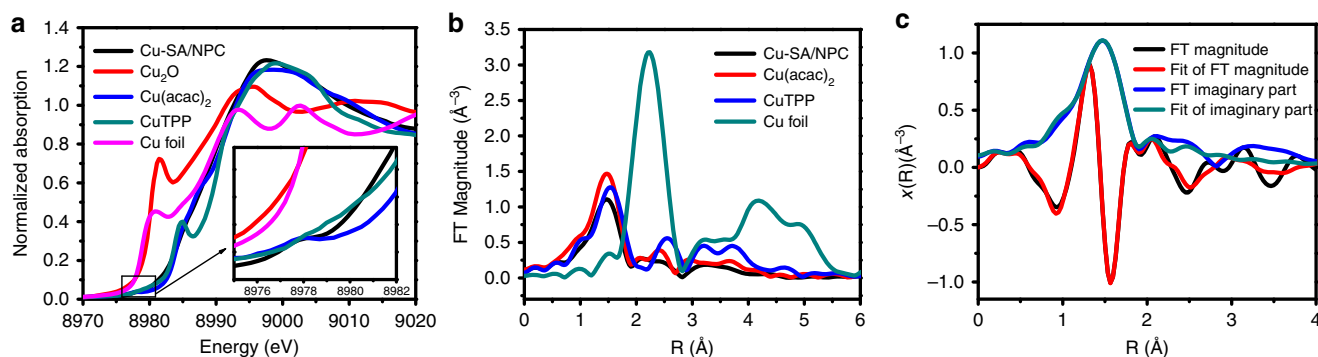


**Fig. 2** Structural characterization of Cu-SA/NPC. **a** Normalized XANES spectra at Cu K-edge of Cu-SA/NPC, Cu<sub>2</sub>O, cupric acetylacetonate (Cu(acac)<sub>2</sub>), copper meso-tetraphenylporphine (CuTPP), and Cu foil. **b** Fourier transforms (FT) magnitude of the experimental EXAFS spectra of Cu-SA/NPC, Cu(acac)<sub>2</sub>, CuTPP, and Cu foil. **c** EXAFS R space fitting curves of Cu-SA/NPC.

a rough surface. It is worth noting that no Cu nanoparticles or large clusters were observed in the SEM and TEM images of Cu-SA/NPC catalysts. The presence of Cu on Cu-SA/NPC was confirmed by atomic-resolution high-angle annular dark-field scanning TEM (HAADF-STEM). Fig. 1d, e clearly showed the presence of bright dots that were attributed to the atomically distributed Cu components. The particle size of Cu was measured to be about 0.1 nm, revealing that Cu on Cu-SA/NPC catalysts was present at atom dimension. Energy dispersive X-ray spectroscopy (EDS) mapping analysis in STEM images confirmed the uniform dispersion of Cu, N, and C species in Cu-SA/NPC (Fig. 1f–i and Supplementary Fig. 4), demonstrating that Cu atom was homogeneously distributed on N-doped carbon materials.

The oxidation state and structural information of Cu-SA/NPC were characterized using X-ray absorption near edge spectroscopy (XANES) and extended X-ray absorption fine structure (EXAFS). Fig. 2a depicts the normalized XANES spectra of Cu-SA/NPC and several reference materials, such as Cu<sub>2</sub>O, cupric acetylacetonate (Cu(acac)<sub>2</sub>), copper meso-tetraphenylporphine (CuTPP), and Cu foil. The white-line intensities in these spectra were related to the oxidation states of Cu species. The white-line intensity of Cu-SA/NPC was similar to that of Cu(acac)<sub>2</sub> and CuTPP, indicating that the Cu atoms existed as Cu(II) species. The pre-edge region was also indicative of the Cu oxidation state, as reported earlier that Cu(II) showed a small pre-edge feature while the pre-edge feature was absent for Cu or Cu(I)<sup>28</sup>. As shown in Fig. 2a, a small pre-edge feature was observed for the Cu-SA/NPC sample, confirming the Cu(II) oxidation state in Cu-SA/NPC. The Fourier-transformed EXAFS spectra of Cu-SA/NPC showed a main peak at ~1.5 Å, which could be assigned to the Cu–N bond. Notably, the peak related to Cu–Cu bond at ~2.2 Å was absent (Fig. 2b), consistent with the presence of individually distributed Cu. According to the EXAFS fitting results (Fig. 2c and Supplementary Table 2), the Cu atom coordinated with N atom and the coordination number was 3.8 ± 0.2. Based on the combined HAADF-STEM and EXAFS results, it could be concluded that the Cu species was atomically dispersed and was fourfold coordinated with N atoms in Cu-SA/NPC<sup>29</sup>.

**Electrochemical reduction of CO<sub>2</sub> on Cu-SA/NPC.** The CO<sub>2</sub> reduction activity of Cu-SA/NPC was investigated by linear sweep voltammetry (LSV) measurements. The LSV tests were performed in a phosphate buffer (0.2 M, pH 6.8) saturated with CO<sub>2</sub> or Ar. As shown in Fig. 3a, the current density in CO<sub>2</sub>-saturated solution was greater than that in Ar-saturated solution for both NPC and Cu-SA/NPC, demonstrating that NPC and Cu-SA/NPC were active for CO<sub>2</sub> electrochemical reduction. The current density for

CO<sub>2</sub> reduction on Cu-SA/NPC was much higher than that on NPC. Moreover, the onset potential (CO<sub>2</sub> reduction current density achieved 1.0 mA cm<sup>-2</sup>) for CO<sub>2</sub> reduction on Cu-SA/NPC was -0.25 V, which was more positive than that on NPC (-0.62 V). These results suggested that the incorporation of single atom Cu into NPC material could significantly enhance its catalytic activity toward CO<sub>2</sub> reduction.

Electrochemical reduction of CO<sub>2</sub> was performed in a CO<sub>2</sub>-saturated 0.1 M KHCO<sub>3</sub> solution (pH 6.8) at applied potential of -0.16 to -0.96 V versus reversible hydrogen electrode (RHE). The detected liquid products on Cu-SA/NPC were formic acid (HCOOH), acetic acid (CH<sub>3</sub>COOH), methanol (CH<sub>3</sub>OH), ethanol (C<sub>2</sub>H<sub>5</sub>OH), and acetone (CH<sub>3</sub>COCH<sub>3</sub>), while the gaseous products were H<sub>2</sub> and CO. Fig. 3b showed the product distribution on Cu-SA/NPC, which was found to be dependent on the applied potential (its current–time curves were presented in Supplementary Fig. 5). It is worthy to note that oxygenate products were generated at a low potential of -0.16 V versus RHE, revealing that the overpotential for CH<sub>3</sub>OH, C<sub>2</sub>H<sub>5</sub>OH, and CH<sub>3</sub>COCH<sub>3</sub> production on Cu-SA/NPC was about 180, 250, and 250 mV, respectively. Among these reduction products, the CH<sub>3</sub>COCH<sub>3</sub> was the major reduced product of CO<sub>2</sub> reduction on the Cu-SA/NPC catalyst at low potential. Moreover, the production rate of CH<sub>3</sub>COCH<sub>3</sub> was further investigated in the potentials between -0.1 and -1.0 V (Supplementary Fig. 6). At the potential of -0.1 V, no CH<sub>3</sub>COCH<sub>3</sub> was detected. The production rate of CH<sub>3</sub>COCH<sub>3</sub> increased at potentials between -0.16 and -0.76 V, and then decreased with the applied potential further negatively shifted to -1.0 V, likely due to the competing reaction of H<sub>2</sub> evolution. The maximum CH<sub>3</sub>COCH<sub>3</sub> production rate reached 336.1 μg h<sup>-1</sup> (-0.76 V), which was 4.3, 2.8, 16.9, and 12.8 times larger than that of HCOOH, CH<sub>3</sub>COOH, CH<sub>3</sub>OH, and C<sub>2</sub>H<sub>5</sub>OH, respectively. No liquid products were detected during the electrolysis in Ar-saturated solution on Cu-SA/NPC catalysts, confirming that the oxygenates were generated from CO<sub>2</sub> electrochemical reduction (Supplementary Fig. 7). As shown in Supplementary Fig. 8, no peak associated with acetone was detected from <sup>1</sup>H NMR spectra after reducing HCOOH or CH<sub>3</sub>COOH in 0.1 M KHCO<sub>3</sub> electrolyte, suggesting that the formed HCOOH and CH<sub>3</sub>COOH products could not be further reduced to acetone on Cu-SA/NPC. The isotope experiment using <sup>13</sup>CO<sub>2</sub> gas as carbon source was conducted and products were analyzed by GC-MS (Supplementary Fig. 9). The peaks at *m/z* = 59 and *m/z* = 60 were characteristic peak of <sup>13</sup>C-labeled CH<sub>3</sub>COCH<sub>3</sub>, which confirmed that the gas <sup>13</sup>CO<sub>2</sub> was reduced on Cu-SA/NPC catalyst. The peak at *m/z* = 61 was not observed, which may be caused by the participation of HCO<sub>3</sub><sup>-</sup> electrolyte in

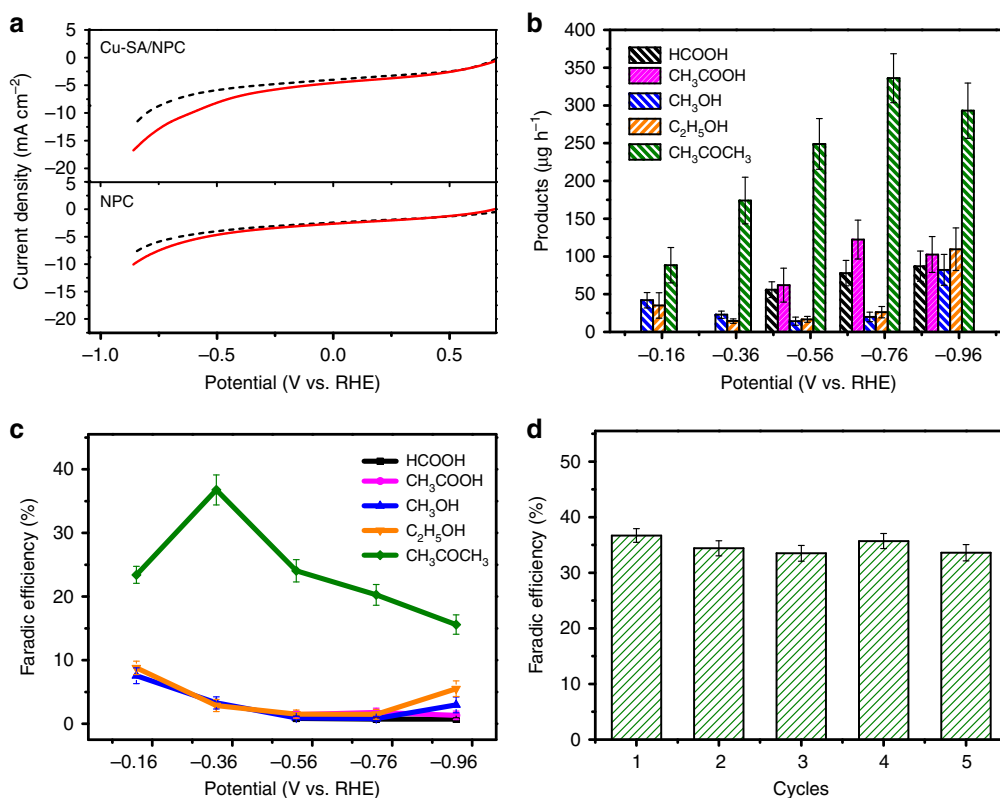


**Fig. 3** Catalytic performance of Cu-SA/NPC. **a** LSV curves of NPC and Cu-SA/NPC. **b** Production rate of CO<sub>2</sub> reduction products on Cu-SA/NPC. **c** Faradaic efficiency of CO<sub>2</sub> reduction products on Cu-SA/NPC. **d** Stability of Cu-SA/NPC.

CO<sub>2</sub> reduction and it was evidenced by the isotope experiment using H<sup>13</sup>CO<sub>3</sub><sup>-</sup> (Supplementary Fig. 10). As shown in Supplementary Fig. 11, the characteristic peaks of CH<sub>3</sub>OH ( $m/z = 31$  and  $m/z = 32$ ), and C<sub>2</sub>H<sub>5</sub>OH ( $m/z = 27$ ,  $m/z = 28$ , and  $m/z = 29$ ) were detected in <sup>13</sup>CO<sub>2</sub> and H<sup>13</sup>CO<sub>3</sub><sup>-</sup>. These results were consistent with those reported in the literature<sup>30,31</sup>. According to the previous studies, there should be a dynamic equilibrium between CO<sub>2</sub> partial pressure and HCO<sub>3</sub><sup>-</sup> concentration and the CO<sub>2</sub> in equilibrium with HCO<sub>3</sub><sup>-</sup> was the source for CO<sub>2</sub> reduction reaction<sup>30,31</sup>.

Energy efficiency was a major consideration for converting CO<sub>2</sub> into chemicals by the electrochemical method, and thus the Faradaic efficiency for CO<sub>2</sub> reduction on Cu-SA/NPC was investigated. As shown in Fig. 3c, the Faradaic efficiency of CH<sub>3</sub>COCH<sub>3</sub> generation was 15.6–36.7% at the applied potential range of -0.16 to -0.96 V, which was much higher than those of other oxygenate products at tested potentials. With the applied potential negatively shifted, the Faradaic efficiency of CH<sub>3</sub>COCH<sub>3</sub> generation increased and reached to a maximum value of 36.7% at -0.36 V, which was 11.2 and 12.7 times as great as those for CH<sub>3</sub>OH and C<sub>2</sub>H<sub>5</sub>OH, respectively. Both the production rate and Faradaic efficiency of acetone generation on Cu-SA/NPC were significantly enhanced as compared with other electrocatalysts reported in the literature<sup>32,33</sup> (Supplementary Table 3). The stability of the Cu-SA/NPC catalyst was measured by five sequential CO<sub>2</sub> electroreduction experiments at -0.36 V (Fig. 3d). The Faradaic efficiency for CH<sub>3</sub>COCH<sub>3</sub> generation remained at ~36.7% for each cycle. Furthermore, the catalysts were characterized by SEM and HAADF-STEM (Supplementary Fig. 12) after five sequential CO<sub>2</sub> reduction. The rhombic dodecahedral morphology of the post-reaction catalysts was intact. The HAADF-STEM results showed that Cu remained atomically distributed in porous carbon. These results indicated

that the Cu-SA/NPC catalyst showed good stability in CO<sub>2</sub> electrochemical reduction.

The reduced products for the electrochemical reduction of CO<sub>2</sub> on NPC were measured for comparison. As shown in Supplementary Fig. 13, the products on NPC were detected to be HCOOH and CH<sub>3</sub>COOH at tested potentials. The trace amount of Zn impurity should have a negligible effect on acetone production from CO<sub>2</sub> reduction on Cu-SA/NPC, as discussed in the Supplementary Note 1. Such comparison suggested that the production of CH<sub>3</sub>OH, C<sub>2</sub>H<sub>5</sub>OH, and CH<sub>3</sub>COCH<sub>3</sub> on Cu-SA/NPC was attributed to the presence of single atom Cu. The Cu-SA/NPC catalysts with different Cu content were prepared. The Cu-SA/NPC catalyst was synthesized with the Zn/Cu ratio of 10/1. The catalysts with Zn/Cu ratios of 20/1, 5/1, 10/3, and 5/3 were also synthesized and denoted as Cu-SA/NPC<sub>0.5</sub>, Cu-SA/NPC<sub>2</sub>, Cu-SA/NPC<sub>3</sub>, and Cu-SA/NPC<sub>6</sub>, respectively. As shown in Supplementary Fig. 14, the Cu-SA/NPC<sub>0.5</sub>, Cu-SA/NPC<sub>2</sub>, and Cu-SA/NPC<sub>3</sub> retained the rhombic dodecahedral morphology of pristine ZIF-8, and the size of prepared catalysts increased with increasing Cu content. The pristine rhombic dodecahedral morphology was destroyed when further increased the Cu content to a Zn/Cu ratio of 5/3 (Cu-SA/NPC<sub>6</sub>). Therefore, the CO<sub>2</sub> electroreduction was conducted on Cu-SA/NPC<sub>0.5</sub>, Cu-SA/NPC, Cu-SA/NPC<sub>2</sub>, and Cu-SA/NPC<sub>3</sub> at -0.76 V (Supplementary Fig. 15), with a acetone production rate of 108.6, 336.1, 194.7, and 129.3 µg h<sup>-1</sup>, respectively. The Faradaic efficiency of acetone generation followed the same trend as Cu-SA/NPC > Cu-SA/NPC<sub>2</sub> > Cu-SA/NPC<sub>3</sub> > Cu-SA/NPC<sub>0.5</sub>. According to the XPS results, the Cu content of Cu-SA/NPC<sub>0.5</sub>, Cu-SA/NPC, Cu-SA/NPC<sub>2</sub>, and Cu-SA/NPC<sub>3</sub> catalysts increased from 0.1 to 0.3% (Supplementary Table 4). However, the N content also increased slightly from 8.3 to 8.4% as the Zn/Cu ratio increased to 10/1, and the N content decreased to 6.4% with further increasing the Zn/Cu ratio to 10/3

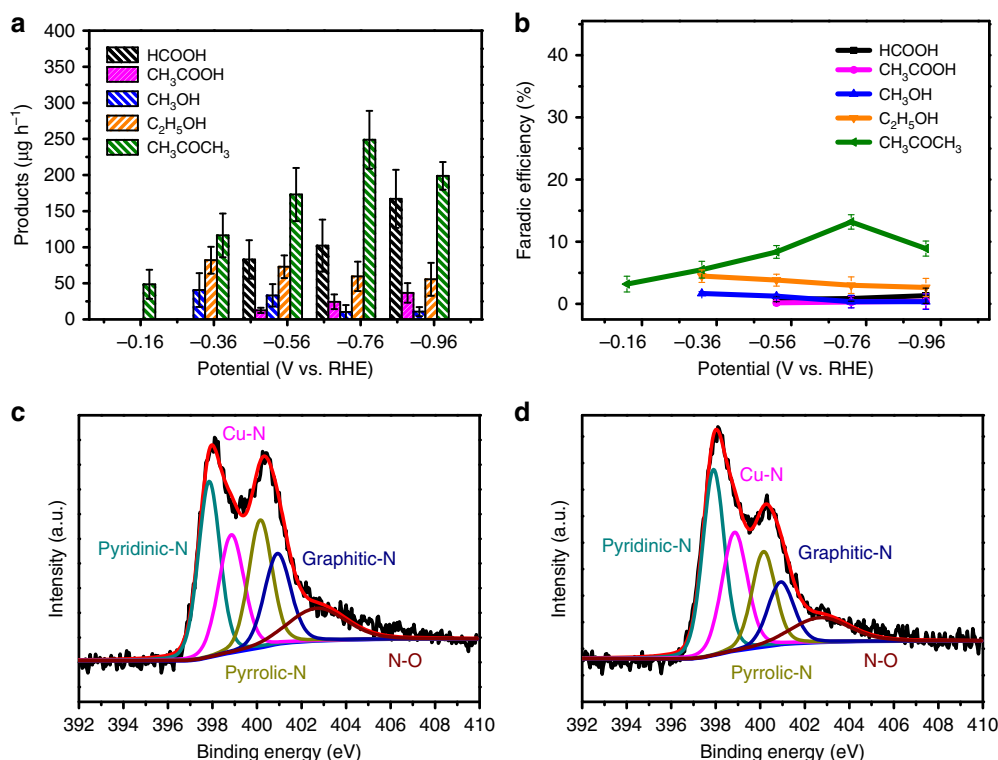


**Fig. 4** Catalytic performance of Cu-SA/NPC<sub>Ar</sub> and high-resolution XPS. **a** Production rate of CO<sub>2</sub> reduction products on Cu-SA/NPC<sub>Ar</sub>. **b** Faradaic efficiency of CO<sub>2</sub> reduction products on Cu-SA/NPC<sub>Ar</sub>. **c** XPS N 1s spectra of Cu-SA/NPC. **d** XPS N 1s spectra of Cu-SA/NPC<sub>Ar</sub>.

(Supplementary Figs. 16, 17 and Table 4). The trend in the change of N content with the doping content of Cu metal was similar to that reported in the literature<sup>34</sup>. Therefore, the acetone production from CO<sub>2</sub> on Cu-SA/NPC was not only related to the atomic Cu doping, but also related to the N content and species.

In order to determine whether the interaction between Cu and supported materials would be influenced by the carbonization conditions of MOFs, the Cu catalyst was prepared under Ar atmosphere and denoted as Cu-SA/NPC<sub>Ar</sub>. According to the LSV results (Supplementary Fig. 18), the onset potential for CO<sub>2</sub> reduction on Cu-SA/NPC (−0.25 V) was more positive than that on Cu-SA/NPC<sub>Ar</sub> (−0.38 V), indicating that CO<sub>2</sub> reduction occurred more easily on the Cu-SA/NPC electrocatalyst. The production rate and Faradaic efficiency of reduced products from CO<sub>2</sub> reduction on Cu-SA/NPC<sub>Ar</sub> were also measured for comparison (Fig. 4a, b). At the applied potential of −0.76 V, the CH<sub>3</sub>COCH<sub>3</sub> production rate on Cu-SA/NPC was about 336.1 μg h<sup>−1</sup> with a Faradaic efficiency of 20.3%, while Cu-SA/NPC<sub>Ar</sub> exhibited lower CH<sub>3</sub>COCH<sub>3</sub> production rate (248.8 μg h<sup>−1</sup>) and Faradaic efficiency (13.2%), indicating that Cu-SA/NPC possessed a better CO<sub>2</sub> reduction activity than Cu-SA/NPC<sub>Ar</sub>. Since the Cu-SA/NPC and Cu-SA/NPC<sub>Ar</sub> catalysts had similar Cu content, BET surface area, and pore structure (Supplementary Tables 1, 5 and Figs. 19, 20), the different CO<sub>2</sub> reduction activity may be resulted from the content and type of N species. The N content was characterized by X-ray photoelectron spectroscopy (XPS) and the N composition was determined by the peak area ratio of different N species (details provided in the Supplementary methods). Based on the XPS results, the Cu-SA/NPC and Cu-SA/NPC<sub>Ar</sub> showed a similar total N content, while the distribution of N species was different (Supplementary Table 4). Fig. 4c, d showed the XPS N 1s spectra of Cu-SA/NPC and Cu-SA/NPC<sub>Ar</sub>, respectively. Both spectra exhibited five peaks with binding energies at 397.9, 398.9, 400.2, 401.0, and 402.7 eV, which were assigned to pyridinic N, metal Cu–N, pyrrolic N, graphite N, and

oxidized N (N–O), respectively<sup>35,36</sup>. The content of graphite N and metal Cu–N was similar, while that of pyridinic N, pyrrolic N, and oxidized N (N–O) was different. As shown in Supplementary Table 4, the NPC possessed the oxidized N content of 1.1%, similar to that of Cu-SA/NPC (1.2%). However, there was no acetone production from CO<sub>2</sub> reduction on NPC without Cu (Supplementary Fig. 13), suggesting the oxidized N alone might not play an important role in acetone production. As shown in Supplementary Table 4, the content of pyridinic N and pyrrolic N on Cu-SA/NPC was 2.2% and 1.8%, respectively, while that on Cu-SA/NPC<sub>Ar</sub> was 2.7% and 1.4%, respectively. This comparison indicated that the Cu-SA/NPC had a higher content of pyrrolic N than that of Cu-SA/NPC<sub>Ar</sub>, which might play an important role for acetone production on Cu-SA/NPC. In view of CO<sub>2</sub> reduction measurements and XPS results, the CH<sub>3</sub>COCH<sub>3</sub> production from CO<sub>2</sub> reduction might be determined by the single atom Cu and the content of pyrrolic N. However, how these two species combined with each other was not confirmed based on experimental results and DFT calculations were conducted to identify the active sites of Cu-SA/NPC and to uncover the mechanisms for acetone production from CO<sub>2</sub> reduction.

**Active sites identification and mechanisms.** As the electrocatalytic activity of SAC could be affected by the coordination environment of isolated metal atoms<sup>37</sup>, different types of coordinated N species were first examined. According to the combined HAADF-STEM and EXAFS results, the Cu species should be atomically dispersed and was fourfold coordinated with N atoms in the Cu-SA/NPC<sup>29</sup> catalyst. Herein, two catalyst models were constructed, in which single atom Cu was doped into a graphitic sheet with coordination environments with four pyridine N atoms (Cu-pyridinic-N<sub>4</sub> site) and four pyrrole N atoms (Cu-pyrrolic-N<sub>4</sub> site) (inside the Fig. 5a). The Gibbs free energy diagrams of CO<sub>2</sub> reduction and ΔG values of elementary steps

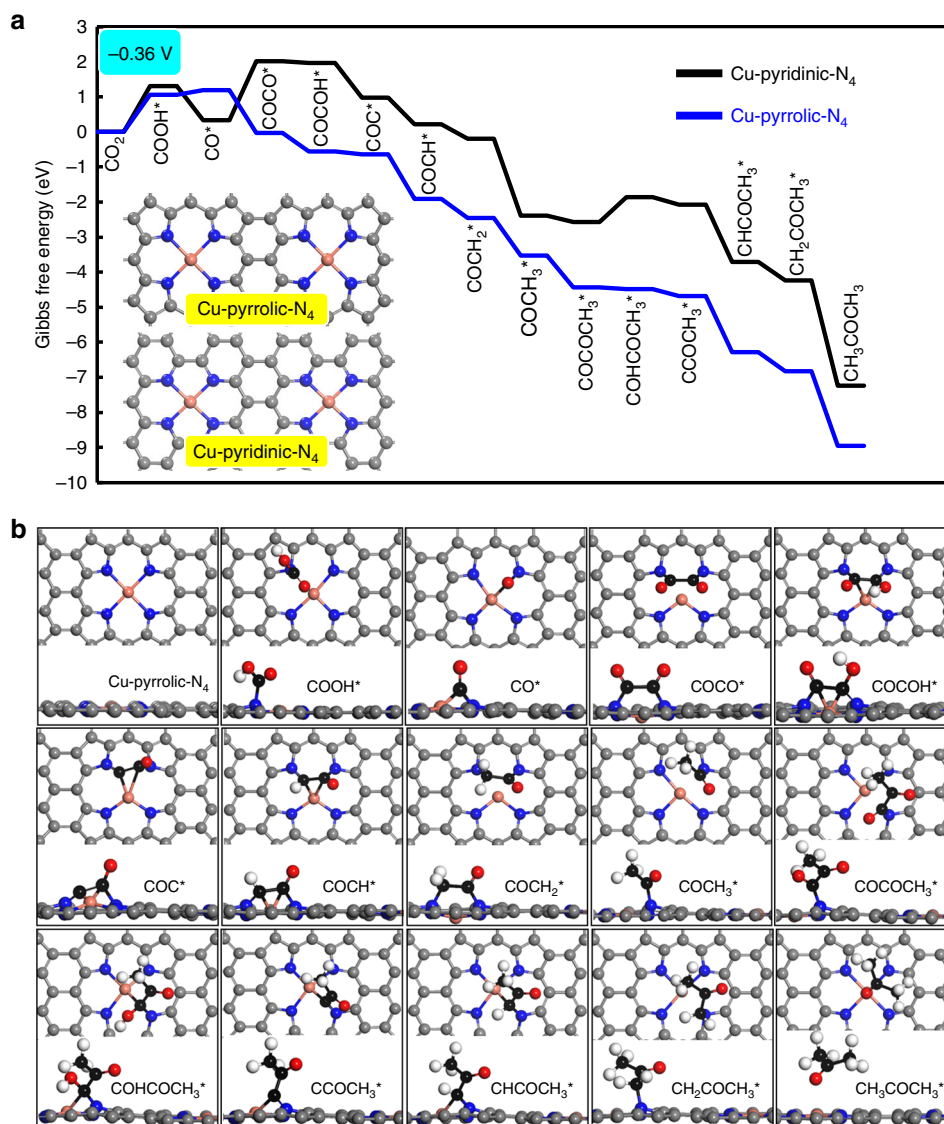


**Fig. 5** DFT calculations of reaction pathways on different Cu-N sites of Cu-SA/NPC. **a** Free energy diagrams calculated at a potential of  $-0.36$  V for  $\text{CO}_2$  reduction to  $\text{CH}_3\text{COCH}_3$  on Cu-pyridinic- $\text{N}_4$  and Cu-pyrrolic- $\text{N}_4$  sites of Cu-SA/NPC (the computational models were included in the figure). **b** Optimized structures of all reaction intermediates involved in the pathways of  $\text{CO}_2$  reduction on the Cu-pyrrolic- $\text{N}_4$  site (gray: C of catalyst; black: C of adsorbate; red: O; orange: Cu; blue: N; white: H).

involved were calculated based on the computational hydrogen electrode model. Fig. 5a illustrated the lowest energy pathways of  $\text{CH}_3\text{COCH}_3$  formation from  $\text{CO}_2$  reduction on Cu-pyridinic- $\text{N}_4$  and Cu-pyrrolic- $\text{N}_4$  sites of Cu-SA/NPC at a potential of  $-0.36$  V versus RHE. The free energy diagrams at 0 V on the two sites were provided in Supplementary Fig. 21. Fig. 5b showed the optimized structures of all states generated on the Cu-pyrrolic- $\text{N}_4$  site of Cu-SA/NPC while the optimized structures formed on Cu-pyridinic- $\text{N}_4$  were provided in Supplementary Fig. 22. The proposed path went through in the sequence of  $\text{CO}_2 \rightarrow \text{COOH}^* \rightarrow \text{CO}^* \rightarrow \text{COCO}^* \rightarrow \text{COCO}^* \rightarrow \text{COC}^* \rightarrow \text{COCH}^* \rightarrow \text{COCH}_2^* \rightarrow \text{COCH}_3^* \rightarrow \text{COCOCH}_3^* \rightarrow \text{COHCOCH}_3^* \rightarrow \text{COCOCH}_3^* \rightarrow \text{CHCOCH}_3^* \rightarrow \text{CH}_2\text{COCH}_3^* \rightarrow \text{CH}_3\text{COCH}_3$ . The free energy change for the overall process of  $\text{CH}_3\text{COCH}_3$  production from  $\text{CO}_2$  reduction was negative, indicating that reducing  $\text{CO}_2$  to  $\text{CH}_3\text{COCH}_3$  was thermodynamically favorable on the Cu-SA/NPC catalyst. The elementary steps for  $\text{CO}_2$  reduction to  $\text{CH}_3\text{COCH}_3$  were more thermodynamically downhill when a  $-0.36$  V potential was applied (comparing Fig. 5a and Supplementary Fig. 21), indicating that the  $\text{CH}_3\text{COCH}_3$  formation from

$\text{CO}_2$  reduction became more favorable under the electroreduction environment. According to the literature, a rate-limiting step for  $\text{CO}_2$  reduction was the activation of  $\text{CO}_2$  molecule to form a  $\text{COOH}^*$  intermediate via the single electron transfer pathway<sup>38–41</sup>, which was the first step in  $\text{CO}_2$  reduction. In the current DFT calculation, the  $\Delta G$  value calculated at  $-0.36$  V for  $\text{COOH}^*$  formation on Cu-pyrrolic- $\text{N}_4$  was 1.06 eV, being lower than that obtained on Cu-pyridinic- $\text{N}_4$  (1.30 eV) and indicating that  $\text{CO}_2$  reduction should be more facile on the Cu-pyrrolic- $\text{N}_4$  site of Cu-SA/NPC. The  $\text{COOH}^*$  intermediate was reduced to  $\text{CO}^*$  species by reacting with a proton and releasing a  $\text{H}_2\text{O}$  molecule. The  $\Delta G$  values were 0.14 and  $-0.97$  eV for  $\text{CO}^*$  formation on Cu-pyrrolic- $\text{N}_4$  and Cu-pyridinic- $\text{N}_4$  sites, respectively. Based on the lowest energy pathways for  $\text{CH}_3\text{COCH}_3$  generation, the first C–C coupling of two  $\text{CO}^*$  species was crucial for the formation of  $\text{C}_{2+}$  products, and this step was found to have a  $\Delta G$  value of 1.67 eV on Cu-pyridinic- $\text{N}_4$  but was  $-1.23$  eV exothermic on Cu-pyrrolic- $\text{N}_4$ , indicating a quite facile C–C coupling of  $\text{CO}^*$  species catalyzed by the Cu-pyrrolic- $\text{N}_4$  site. Then, the formed  $\text{COCO}^*$  intermediate was reduced to  $\text{COCO}^*$

with a  $\Delta G$  value of  $-0.05$  eV and  $-0.53$  eV on Cu-pyridinic- $N_4$  and Cu-pyrrolic- $N_4$ , respectively. The formation of  $\text{COCO}^*$  species was also reported by Goddard III et al., which was considered as a key intermediate for  $C_2$  or  $C_3$  product formation from  $\text{CO}_2$  reduction<sup>42</sup>. The  $\text{COCO}^*$  was converted into the  $\text{COC}^*$  species by breaking the C–O(H) bond, and the formed  $\text{COC}^*$  was further reduced to the  $\text{COCH}_3^*$  intermediate via sequential hydrogenation steps. These steps were all downhill in free energies on the both sites at  $-0.36$  V, as shown in Fig. 5a. The subsequent C–C bond formed by coupling of the  $\text{COCH}_3^*$  intermediate with another adsorbed  $\text{CO}^*$  led to the formation of  $\text{COCOCH}_3^*$  with a  $\Delta G$  value of  $-0.18$  eV on Cu-pyridinic- $N_4$  and  $-0.92$  eV on Cu-pyrrolic- $N_4$ , showing a more favorable formation of  $C_3$  species from  $C_2$  intermediates on the Cu-pyrrolic- $N_4$  site. Subsequent conversions of  $\text{COCOCH}_3^*$  to acetone were all downhill in free energy change on Cu-pyrrolic- $N_4$  whereas the elementary step of  $\text{COCOCH}_3^*$  reduction to  $\text{COHCOCH}_3^*$  still had an endothermic  $\Delta G$  of  $0.70$  eV on Cu-pyridinic- $N_4$ . The free energy calculations revealed that  $\text{CO}_2$  activation to  $\text{COOH}^*$  was the only slow step on Cu-pyrrolic- $N_4$  (Supplementary Table 6), determining the overall rate for  $\text{CH}_3\text{COCH}_3$  production. The C–C coupling reactions were quite facile to occur, leading to a high selectivity to acetone formation on this site. Other possible C–C coupling pathways including  $\text{CO}^*-\text{CHO}^*$  and  $\text{CO}^*-\text{COH}^*$  were also considered on Cu-pyrrolic- $N_4$ , but these routes were found to be energetically unfavorable as compared with the direct coupling of two  $\text{CO}^*$  species (Supplementary Note 2 and Supplementary Fig. 23). In contrast, several steps proceeded slowly on Cu-pyridinic- $N_4$ , including  $\text{CO}_2$  reduction to  $\text{COOH}^*$ ,  $\text{CO}^*-\text{CO}^*$  coupling and  $\text{COCOCH}_3^*$  reduction to  $\text{COHCOCH}_3^*$  (Supplementary Table 6). The C–C coupling was non-electrochemical reaction and could not be facilitated by the applied potential, therefore, the significantly endothermic free energy change ( $\Delta G$  of  $1.67$  eV) in the coupling of two  $\text{CO}^*$  species hindered acetone formation from  $\text{CO}_2$  reduction on the Cu-pyridinic- $N_4$  site. These calculation results revealed that Cu coordinated with pyrrolic N species (Cu-pyrrolic- $N_4$ ) was active for acetone production rather than pyridinic N species.

To examine whether the uncoordinated pyrrolic N species was active toward acetone formation, DFT calculations were performed on two types of uncoordinated pyrrolic N models without Cu, as shown in Supplementary Figs. 24 and 25, and Supplementary Table 7. The free energy diagrams for acetone production from  $\text{CO}_2$  reduction on uncoordinated pyrrolic- $N_1$ , uncoordinated pyrrolic- $N_4$ , and Cu-pyrrolic- $N_4$  at  $0$  V potential were compared in Supplementary Fig. 24. Clearly, the uncoordinated pyrrolic- $N_4$  was not active toward acetone formation due to several uphill elementary steps other than  $\text{CO}_2$  reduction to  $\text{COOH}^*$  ( $\Delta G$  of  $1.35$  eV), such as  $\text{COCO}^*$  reduction to  $\text{COC}^*$  ( $\Delta G$  of  $1.17$  eV),  $\text{COCH}_2^*$  reduction to  $\text{COCH}_3^*$  ( $\Delta G$  of  $1.07$  eV), and  $\text{COCH}_3^*$  coupling with  $\text{CO}^*$  to form  $\text{COCOCH}_3^*$  ( $\Delta G$  of  $1.05$  eV). For the uncoordinated pyrrolic- $N_1$ , although the first step of  $\text{CO}_2$  reduction to  $\text{COOH}^*$  had a smaller  $\Delta G$  value ( $0.75$  eV) than that ( $1.42$  eV) obtained on Cu-pyrrolic- $N_4$ , subsequent  $\text{CO}^*$  formation from  $\text{COOH}^*$  reduction had a larger  $\Delta G$  of  $1.24$  eV. In addition, steps such as  $\text{COCO}^*$  reduction to  $\text{COCO}^*$  and  $\text{COHCOCH}_3^*$  reduction to  $\text{COCOCH}_3^*$  were energetically endothermic with  $\Delta G$  values of  $0.70$  and  $0.97$  eV, respectively, indicating that the uncoordinated pyrrolic- $N_1$  did not have an advantage for acetone production. The comparison results in Supplementary Fig. 24 revealed that Cu single atom coordinated with pyrrolic N species (Cu-pyrrolic- $N_4$ ) was catalytically more active than the uncoordinated pyrrolic N species, and should be responsible for the acetone production from  $\text{CO}_2$  reduction on Cu-SA/NPC. As shown in Supplementary Table 4, other than the difference in the content of

pyridinic N and pyrrolic N, the content of oxidized N was also different on Cu-SA/NPC and Cu-SA/NPC<sub>Ar</sub>. The experimental results on the NPC catalyst without adding Cu showed no acetone formation from  $\text{CO}_2$  reduction, which suggested that the oxidized N should not be the active site for acetone production on Cu-SA/NPC. To further confirm this, DFT calculations of energetic pathways for  $\text{CO}_2$  reduction to acetone on pyridinic- and pyrrolic- $\text{N}=\text{O}$  sites were performed (Supplementary Figs. 26–28), and detailed results were provided in the Supplementary Note 3 and Supplementary Table 8. Since several elementary steps involved in the paths were highly uphill in  $\Delta G$  (Supplementary Fig. 26), the oxidized N sites were not active for acetone formation. Furthermore, the influence of Zn impurity on acetone production from  $\text{CO}_2$  reduction on the Cu-SA/NPC catalyst was also investigated by DFT calculations (Supplementary Figs. 29, 30) which revealed that Zn was not responsible for acetone production from  $\text{CO}_2$  reduction (Supplementary Note 4).

These DFT results revealed that the active sites for acetone synthesis from  $\text{CO}_2$  reduction on Cu-SA/NPC were Cu-pyrrolic- $N_4$ , consistent with the structural prediction of Cu/N coordination environment from EXAFS characterization and the N species identified from XPS. For  $\text{CO}_2$  reduction to acetone, the formation of reaction intermediates required the synergy between Cu and coordinated pyrrolic N species (Fig. 5b), leading to a facile C–C coupling toward  $C_2$  and  $C_3$  species formation (Fig. 5a). The ICP results provided in Supplementary Table 1 revealed that the content of Cu dispersed into the Cu-SA/NPC catalyst was relatively small, and the EXAFS results (Fig. 2b) confirmed that the Cu coordinated with N atom. The combined experimental and DFT studies confirmed that the Cu single atom coordinated with four pyrrolic N (Cu-pyrrolic- $N_4$ ) should be responsible for the acetone production from  $\text{CO}_2$  reduction on Cu-SA/NPC, and therefore were proposed as the active sites.

As observed in Fig. 3b, other oxygenates such as  $\text{HCOOH}$ ,  $\text{CH}_3\text{COOH}$ ,  $\text{CH}_3\text{OH}$ , and  $\text{C}_2\text{H}_5\text{OH}$  were also detected at different potentials. The energetic pathways for the formation of these oxygenates on the Cu-pyrrolic- $N_4$  active site of Cu-SA/NPC were examined by DFT calculations and the results were illustrated in Fig. 6a–d. Optimized structures of all intermediates were provided in Supplementary Figs. 31–34, with the free energy change for each elementary step involved given in Supplementary Table 9. The relative selectivity to acetone versus these oxygenates was evaluated based on DFT results at  $0$  and  $-0.36$  V. For acetone, the rate-determining step was  $\text{CO}_2$  reduction to  $\text{COOH}^*$ , which had a free energy change of  $1.42$  eV at  $0$  V potential. For  $\text{HCOOH}$  formation, the rate-limiting step was  $\text{CO}_2$  reduction to  $\text{HCOO}^*$  with a  $\Delta G$  of  $2.42$  eV, determining the selectivity to formic acid and making it difficult to form at lower potentials. However, the formation of  $\text{CH}_3\text{COOH}$ ,  $\text{CH}_3\text{OH}$  and  $\text{C}_2\text{H}_5\text{OH}$  all went through a  $\text{CO}^*$  intermediate via  $\text{CO}_2 \rightarrow \text{COOH}^* \rightarrow \text{CO}^*$ , similar to that for acetone formation. Therefore, the selectivity determining step for acetone versus other oxygenates should appear after  $\text{CO}^*$  formation, which was found to be the  $\text{COCOCH}_3^*$  reduction to  $\text{COHCOCH}_3^*$  step with a  $\Delta G$  of  $0.32$  eV for acetone formation, the  $\text{CHOH}^*$  reduction to  $\text{CH}^* + \text{H}_2\text{O}(\text{aq})$  step with a  $\Delta G$  of  $1.12$  eV associated with  $\text{CH}_3\text{COOH}$  formation, the  $\text{CH}_2\text{O}^*$  reduction to  $\text{CH}_2\text{OH}^*$  step with a  $\Delta G$  of  $0.17$  eV for  $\text{CH}_3\text{OH}$  formation, and the  $\text{CHOCH}_2\text{OH}^*$  reduction to  $\text{CHOHCH}_2\text{OH}^*$  step with a  $\Delta G$  of  $0.79$  eV in regard to  $\text{C}_2\text{H}_5\text{OH}$  formation, at  $0$  V potential. Since these steps were all electrochemical reactions, the applied potential could drive these steps occurring more facilely. The relative selectivities predicted for these oxygenate products based on reaction free energy calculations at varied potentials ( $0$  and  $-0.36$  V) were illustrated in Fig. 6e, which was generally consistent with the experimental results shown in Fig. 3b. At lower potentials ( $\leq -0.36$  V), the  $\text{HCOOH}$  and  $\text{CH}_3\text{COOH}$  could not be produced

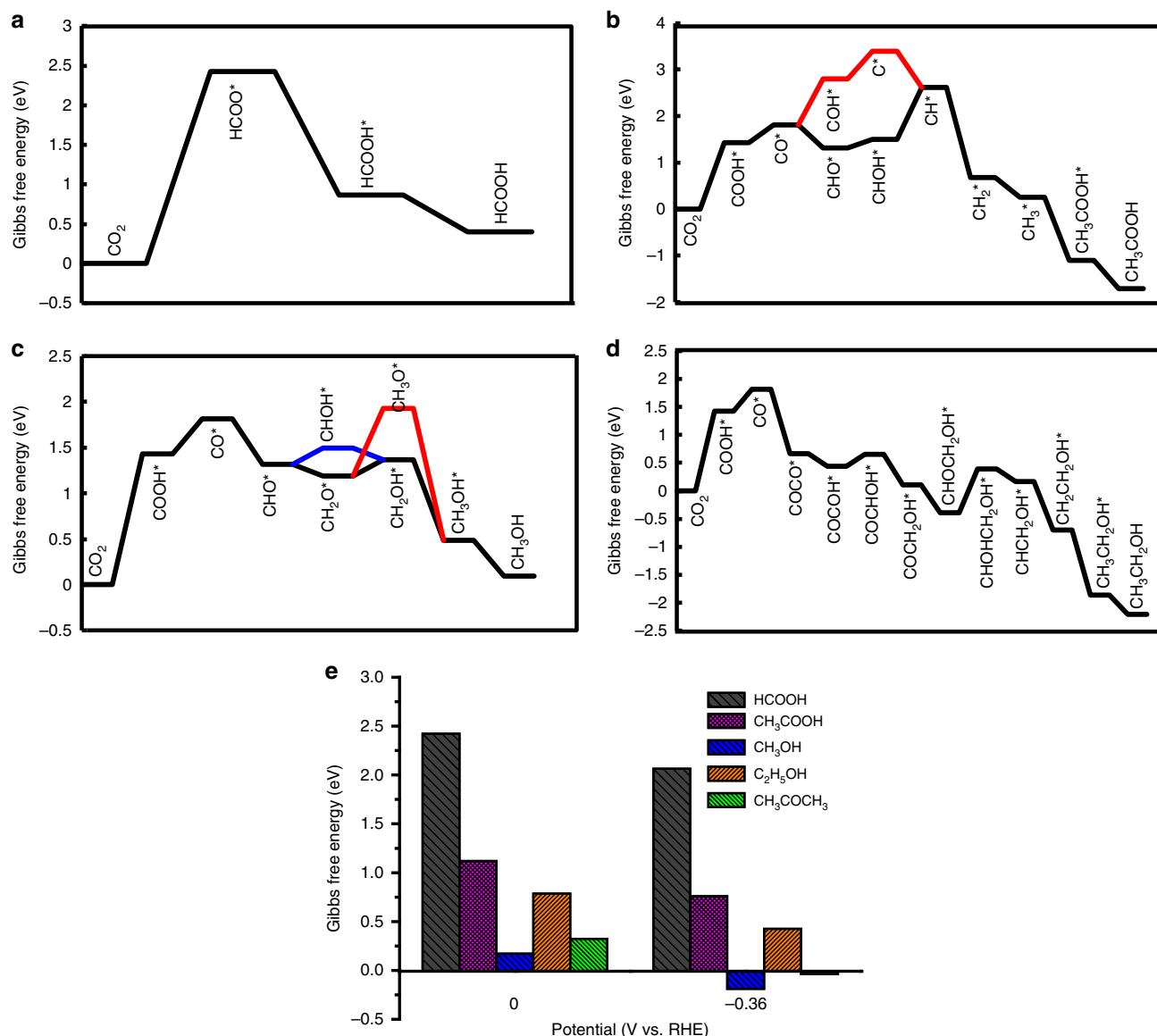


**Fig. 6** Selectivity determination by DFT calculations on Cu-SA/NPC. Free energy diagrams calculated for  $\text{CO}_2$  reduction to **a** HCOOH, **b**  $\text{CH}_3\text{COOH}$ , **c**  $\text{CH}_3\text{OH}$  and **d**  $\text{C}_2\text{H}_5\text{OH}$  at 0 V potential. **e** Relative selectivity evaluation based on DFT calculations on reaction free energies of all oxygenate products on the Cu-pyrrolic- $\text{N}_4$  site of Cu-SA/NPC.

due to higher uphill  $\Delta G$  values; the formation of  $\text{CH}_3\text{COCH}_3$  and  $\text{CH}_3\text{OH}$  was relatively fast because the selectivity determining step became more energetically favorable with the applied potentials; the  $\text{C}_2\text{H}_5\text{OH}$  could be produced but the selectivity should be lower than that of  $\text{CH}_3\text{COCH}_3$  and  $\text{CH}_3\text{OH}$  due to a moderate uphill free energy change of the selectivity determining step when the potential was applied. The higher selectivity toward acetone formation from  $\text{CO}_2$  reduction on the Cu-SA/NPC catalyst should originate from the unique Cu-pyrrolic- $\text{N}_4$  active site in stabilizing the reaction intermediates involved in acetone production as well as facilitating the C-C coupling reactions involved in  $\text{CO}_2$  reduction to acetone. As shown in Fig. 5a, the two C-C coupling steps were largely downhill in free energy change ( $-1.22$  and  $-0.92$  eV, respectively, for  $\text{CO}^*-\text{CO}^*$  and  $\text{CO}^*-\text{COCH}_3^*$  coupling) and the formation of reaction intermediates was energetically quite favorable (except for the first  $\text{CO}_2$  reduction to  $\text{COOH}^*$  step) due to the synergy of Cu-N coordination and interaction with intermediate species for acetone formation on the Cu-pyrrolic- $\text{N}_4$  site of Cu-SA/NPC.

## Discussion

Efficient and selective electrochemical reduction of  $\text{CO}_2$  to  $\text{CH}_3\text{COCH}_3$  was achieved on Cu-SA/NPC. The maximum production rate of  $\text{CH}_3\text{COCH}_3$  was  $336.1 \mu\text{g h}^{-1}$  and the highest Faradaic efficiency of  $\text{CH}_3\text{COCH}_3$  production was 36.7%, significantly enhanced as compared with other electrocatalysts reported in the literature. Based on  $\text{CO}_2$  reduction experiments and DFT calculations, the high activity and selectivity of Cu-SA/NPC for  $\text{CH}_3\text{COCH}_3$  generation were mainly originated from single atom Cu coordinated to four pyrrolic N atoms, which lowered the reaction energies required for  $\text{CO}_2$  activation and C-C bond coupling. The proposed energetically most favorable pathways for  $\text{CH}_3\text{COCH}_3$  generation from  $\text{CO}_2$  reduction went through  $\text{CO}_2 \rightarrow \text{COOH}^* \rightarrow \text{CO}^* \rightarrow \text{COCO}^* \rightarrow \text{COCO}^* \rightarrow \text{COCHO}^* \rightarrow \text{COC}^* \rightarrow \text{COCH}^* \rightarrow \text{COCH}_2^* \rightarrow \text{COCH}_3^* \rightarrow \text{COCOCH}_3^* \rightarrow \text{COHCOCH}_3^* \rightarrow \text{CCOCH}_3^* \rightarrow \text{CHCOCH}_3^* \rightarrow \text{CH}_2\text{COCH}_3^* \rightarrow \text{CH}_3\text{COCH}_3$ . The higher selectivity toward acetone formation from  $\text{CO}_2$  reduction on the Cu-SA/NPC catalyst should originate from the unique Cu-pyrrolic- $\text{N}_4$  active sites in stabilizing the



reaction intermediates involved in acetone production as well as facilitating the C–C coupling reactions due to the Cu–N synergy. This work offers fundamental insight into the design of efficient electrocatalysts for reducing CO<sub>2</sub> to multi-carbon products, which is valuable in the field of energy regeneration and electrochemical synthesis.

## Methods

**Synthesis.** The catalyst was obtained by carbonization of Cu-doped ZIF-8 (Cu-ZIF-8) precursor. For synthesis of Cu-ZIF-8, 5.256 g of 2-methylimidazole was dissolved in 80 mL of methanol (solution A). 4.76 g of Zn(NO<sub>3</sub>)<sub>2</sub>·6H<sub>2</sub>O, and 0.31 g of Cu(CH<sub>3</sub>COO)<sub>2</sub>·H<sub>2</sub>O, were dissolved in 120 mL of methanol (solution B). After ultrasound for 10 min, solution B was added into solution A and the mixed solution was stirred for 30 min at room temperature. Subsequently, the mixture was transferred into Teflon-lined autoclave and heated at 120 °C for 4 h. The products were washed with methanol and DMF several times, and dried at 80 °C under vacuum. The obtained Cu-ZIF-8 powder was carbonized at 1000 °C for 4 h under nitrogen (N<sub>2</sub>) or argon (Ar) atmosphere. The heating rate was set to 5 °C min<sup>-1</sup>. The sample was denoted as Cu-SA/NPC and Cu-SA/NPC<sub>Ar</sub>, respectively. The catalysts with different content of Cu (0.16, 0.62, 0.93, and 1.86 g Cu with Zn/Cu ratios of 20/1, 5/1, 10/3, and 5/3, respectively) were also synthesized and the obtained catalysts were denoted as Cu-SA/NPC<sub>0.5</sub>, Cu-SA/NPC<sub>2</sub>, Cu-SA/NPC<sub>3</sub>, and Cu-SA/NPC<sub>6</sub>, respectively.

**Characterization.** X-ray diffraction (XRD) patterns were measured by a Shimadzu LabX XRD-6000 diffractometer with Cu Kα radiation ( $\lambda = 0.15406$  nm). Scanning electron microscopy (SEM) and transmission electron microscopy (TEM) analyses were performed on a Hitachi S-4800 microscope and an FEI-Tecnaï G<sup>2</sup> 20 microscope, respectively. XPS measurements were conducted by using a VG ESCALAB 250 instrument with a monochromatized Al X-ray source (1486.6 eV). Nitrogen adsorption-desorption isotherms were obtained from a Quadrasorb instrument at 77 K. ICP-AES was detected by a Perkinmer Optima 2000DV instrument. The HAADF-STEM images were obtained on a JEOL ARM200CF fifth order aberration-corrected TEM equipped with a dual-type EDS detector. The X-ray absorption fine structure spectra were measured at the BL8C beamline in Pohang Light Source (PLS), Korea.

**Electrochemical measurements.** Electrochemical measurements were conducted in an airtight double-cell with a 750E electrochemical workstation. The electrolyte of cathode and anode compartments was the same and these two compartments were separated by Nafion N117 membrane. A platinum sheet and saturated calomel electrode (SCE) were served as counter electrode and reference electrode, respectively. Prior to electrochemical reduction of CO<sub>2</sub>, the cathode compartment was bubbled with CO<sub>2</sub> for 30 min and kept being purged with CO<sub>2</sub> during electrocatalytic reduction. The cyclic voltammograms tests were performed on Ar- or CO<sub>2</sub>-saturated electrolyte with a scan rate of 50 mV s<sup>-1</sup>. All the potentials were converted to the RHE using equation as:  $E_{(\text{vs. RHE})} = E_{(\text{vs. SCE})} + 0.0591 \times \text{pH} + 0.241$  V.

**DFT calculations.** All calculations were conducted by using the Vienna Ab-initio Simulation Package<sup>43,44</sup>. The exchange-correlation energies were treated with the spin-polarized generalized gradient approximation and Perdew–Bruke–Ernzerh of functional<sup>45</sup>. Core electrons were represented by projector augmented-wave pseudopotentials<sup>46</sup>. A 400 eV plane wave cutoff energy and a  $2 \times 2 \times 1$  k-point sampling were used for all calculations. The Cu single atom doped in graphite sheet with coordination environments of four pyridine nitrogen atoms and four pyrrole nitrogen atoms were constructed and denoted as Cu-pyridinic-N<sub>4</sub> and Cu-pyrrolic-N<sub>4</sub>, respectively. The computational hydrogen electrode model<sup>47,48</sup> was utilized to calculate the free energies of intermediates involved in CO<sub>2</sub> reduction under experimental conditions.

## Data availability

The authors declare that all data supporting the results of this study are available within the paper and its supplementary information files or from the corresponding authors upon reasonable request.

## Code availability

All codes are available upon reasonable request.

Received: 24 October 2019; Accepted: 29 April 2020;

Published online: 15 May 2020

## References

- Hoang, T. T. H., Verma, S., Ma, S., Fister, T. T., Timoshenko, J., Frenkel, A. I., Kenis, P. J. A. & Gewirth, A. A. Nanoporous copper-silver alloys by additive-controlled electrodeposition for the selective electroreduction of CO<sub>2</sub> to ethylene and ethanol. *J. Am. Chem. Soc.* **140**, 5791–5797 (2018).
- Ju, W., Bagger, A., Hao, G.-P., Varela, A. S., Sinev, I., Bon, V., Roldan Cuenya, B., Kaskel, S., Rossmel, J. & Strasser, P. Understanding activity and selectivity of metal-nitrogen-doped carbon catalysts for electrochemical reduction of CO<sub>2</sub>. *Nat. Commun.* **8**, 944 (2017).
- Zhu, W., Tackett, B. M. & Chen, J. G. et al. Bimetallic electrocatalysts for CO<sub>2</sub> reduction. *Top. Curr. Chem.* **376**, 41 (2018).
- Zhu, D. D., Liu, J. L. & Qiao, S. Z. Recent advances in inorganic heterogeneous electrocatalysts for reduction of carbon dioxide. *Adv. Mater.* **28**, 3423–3452 (2016).
- Morales-Guio, C. G., Cave, E. R., Nitopi, S. A., Feaster, J. T., Wang, L., Kuhl, K. P., Jackson, A., Johnson, N. C., Abram, D. N., Hatsukade, T., Hahn, C. & Jaramillo, T. F. Improved CO<sub>2</sub> reduction activity towards C<sub>2+</sub> alcohols on a tandem gold on copper electrocatalyst. *Nat. Catal.* **1**, 764–771 (2018).
- Liang, Z.-Q., Zhuang, T.-T., Seifitokaldani, A., Li, J., Huang, C.-W., Tan, C.-S., Li, Y., De Luna, P., Dinh, C. T., Hu, Y., Xiao, Q., Hsieh, P.-L., Wang, Y., Li, F., Quintero-Bermudez, R., Zhou, Y., Chen, P., Pang, Y., Lo, S.-C., Chen, L.-J., Tan, H., Xu, Z., Zhao, S., Sinton, D. & Sargent, E. H. Copper-on-nitride enhances the stable electroreduction of multi-carbon products from CO<sub>2</sub>. *Nat. Commun.* **9**, 3828 (2018).
- Zhuang, T.-T., Liang, Z.-Q., Seifitokaldani, A., Li, Y., De Luna, P., Burdyny, T., Che, F., Meng, F., Min, Y., Quintero-Bermudez, R., Dinh, C. T., Pang, Y., Zhong, M., Zhang, B., Li, J., Chen, P.-N., Zheng, X.-L., Liang, H., Ge, W.-N., Ye, B.-J., Sinton, D., Yu, S.-H. & Sargent, E. H. Steering post-C–C coupling selectivity enables high efficiency electroreduction of carbon dioxide to multi-carbon alcohols. *Nat. Catal.* **1**, 421–428 (2018).
- Wang, L. X., Wang, L., Liu, X. L., Wang, H., Zhang, W., Yang, Q., Ma, J. Y., Dong, X., Yoo, S. J., Kim, J.-G., Meng, X. J. & Xiao, F.-S. Selective hydrogenation of CO<sub>2</sub> to ethanol over cobalt catalysts. *Angew. Chem.* **130**, 6212–6216 (2018).
- Zhou, Y., Che, F., Liu, M., Zou, C., Liang, Z., De Luna, P., Yuan, H., Li, J., Wang, Z., Xie, H., Li, H., Chen, P., Bladt, E., Quintero-Bermudez, R., Sham, T.-K., Bals, S., Hofkens, J., Sinton, D., Chen, G. & Sargent, E. H. Dopant-induced electron localization drives CO<sub>2</sub> reduction to C<sub>2</sub> hydrocarbons. *Nat. Chem.* **10**, 974–980 (2018).
- Varela, A. S., Ranjbar, S. N., Steinberg, J., Ju, W., Oh, H.-S. & Strasser, P. Metal-doped nitrogenated carbon as an efficient catalyst for direct CO<sub>2</sub> electroreduction to CO and hydrocarbons. *Angew. Chem. Int. Ed.* **54**, 10758–10762 (2015).
- Zheng, X., Ji, Y., Tang, J., Wang, J., Liu, B., Steinrück, H.-G., Lim, K., Li, Y., Toney, M. F., Chan, K. & Cui, Y. Theory-guided Sn/Cu alloying for efficient CO<sub>2</sub> electroreduction at low overpotentials. *Nat. Catal.* **2**, 55–61 (2019).
- Ren, D., Deng, Y., Handoko, A. D., Chen, C. S., Malkhandi, S. & Yeo, B. S. Selective electrochemical reduction of carbon dioxide to ethylene and ethanol on copper(I) oxide catalysts. *ACS Catal.* **5**, 2814–2821 (2015).
- Genovese, C., Ampelli, C., Perathoner, S. & Centi, G. Electrocatalytic conversion of CO<sub>2</sub> on carbon nanotube-based electrodes for producing solar fuels. *J. Catal.* **308**, 237–249 (2013).
- Li, W. Electrocatalytic reduction of CO<sub>2</sub> to small organic molecule fuels on metal catalysts. *Advances in CO<sub>2</sub> conversion and utilization*. (American Chemical Society, USA, 2010).
- Handoko, A. D., Chan, K. W. & Yeo, B. S. -CH<sub>3</sub> mediated pathway for the electroreduction of CO<sub>2</sub> to ethane and ethanol on thick oxide-derived copper catalysts at low overpotentials. *ACS Energy Lett.* **2**, 2103–2109 (2017).
- Lee, S., Park, G. & Lee, J. Importance of Ag-Cu biphasic boundaries for selective electrochemical reduction of CO<sub>2</sub> to ethanol. *ACS Catal.* **7**, 8594–8604 (2017).
- Hori, Y., Takahashi, I., Koga, O. & Hoshi, N. Selective formation of C<sub>2</sub> compounds from electrochemical reduction of CO<sub>2</sub> at a series of copper single crystal electrodes. *J. Phys. Chem. B* **106**, 15–17 (2002).
- Benson, E. E., Kubiak, C. P., Sathrum, A. J. & Smieja, J. M. Electrocatalytic and homogeneous approaches to conversion of CO<sub>2</sub> to liquid fuels. *Chem. Soc. Rev.* **38**, 89–99 (2009).
- Choi, J., Kim, J., Wagner, P., Gambhir, S., Jalili, R., Byun, S., Sayyar, S., Lee, Y. M., MacFarlane, D. R., Wallace, G. G. & Officer, D. L. Energy efficient electrochemical reduction of CO<sub>2</sub> to CO using a three-dimensional porphyrin/graphene hydrogel. *Energy Environ. Sci.* **12**, 747–755 (2019).
- Fan, Q., Zhang, M., Jia, M., Liu, S., Qiu, J. & Sun, Z. Electrochemical CO<sub>2</sub> reduction to C<sub>2+</sub> species: heterogeneous electrocatalysts, reaction pathways, and optimization strategies. *Mater. Today Energy* **10**, 280–301 (2018).
- Jiang, K., Sandberg, R. B., Akey, A. J., Liu, X., Bell, D. C., Nørskov, J. K., Chan, K. & Wang, H. Metal ion cycling of Cu foil for selective C–C coupling in electrochemical CO<sub>2</sub> reduction. *Nat. Catal.* **1**, 111–119 (2018).

22. Chen, J. G. Electrochemical CO<sub>2</sub> reduction via low-valent nickel single-atom catalyst. *Joule* **2**, 587–589 (2018).
23. Wang, A., Li, J. & Zhang, T. Heterogeneous single-atom catalysis. *Nat. Rev. Chem.* **2**, 65–81 (2018).
24. Chen, Y., Ji, S., Chen, C., Peng, Q., Wang, D. & Li, Y. Single-atom catalysts: synthetic strategies and electrochemical applications. *Joule* **2**, 1242–1264 (2018).
25. Gao, S., Lin, Y., Jiao, X., Sun, Y., Luo, Q., Zhang, W., Li, D., Yang, J. & Xie, Y. Partially oxidized atomic cobalt layers for carbon dioxide electroreduction to liquid fuel. *Nature* **529**, 68–71 (2016).
26. Yang, H. B., Hung, S.-F., Liu, S., Yuan, K., Miao, S., Zhang, L., Huang, X., Wang, H.-Y., Cai, W., Chen, R., Gao, J., Yang, X., Chen, W., Huang, Y., Chen, H. M., Li, C. M., Zhang, T. & Liu, B. Atomically dispersed Ni(I) as the active site for electrochemical CO<sub>2</sub> reduction. *Nat. Energy* **3**, 140–147 (2018).
27. Genovese, C., Schuster, M. E., Gibson, E. K., Gianolio, D., Posligua, V., Graucrespo, R., Cibin, G., Wells, P. P., Garai, D., Solokha, V., Krick Calderon, S., Velasco-Velez, J. J., Ampelli, C., Perathoner, S., Held, G., Centi, G. & Arrigo, R. Operando spectroscopy study of the carbon dioxide electro-reduction by iron species on nitrogen-doped carbon. *Nat. Commun.* **9**, 935 (2018).
28. Zhang, G. H., Yi, H., Zhang, G. T., Deng, Y., Bai, R. P., Zhang, H., Miller, J. T., Kropf, A. J., Bunel, E. E. & Lei, A. W. Direct observation of reduction of Cu(II) to Cu(I) by terminal alkynes. *J. Am. Chem. Soc.* **136**, 924–926 (2014).
29. Chen, Y. J., Ji, S. F., Wang, Y. G., Dong, J. C., Chen, W. X., Li, Z., Shen, R. G., Zheng, L. R., Zhuang, Z. B., Wang, D. S. & Li, Y. D. Isolated single iron atoms anchored on N-doped porous carbon as an efficient electrocatalyst for the oxygen reduction reaction. *Angew. Chem.* **129**, 1–6 (2017).
30. Zhu, S. Q., Li, T. H., Cai, W. B. & Shao, M. H. CO<sub>2</sub> electrochemical reduction as probed through infrared spectroscopy. *ACS Energy Lett.* **4**, 682–689 (2019).
31. Guo, Y., Shi, W. J., Yang, H. J., He, Q. F., Zeng, Z. M., Ye, J.-Y., He, X. R., Huang, R. Y., Wang, C. & Lin, W. B. Cooperative stabilization of the [pyridinium-CO<sub>2</sub>-Co] adduct on a metal-organic layer enhances electrocatalytic CO<sub>2</sub> reduction. *J. Am. Chem. Soc.* **141**, 17875–17883 (2019).
32. Jung, H., Lee, S. Y., Lee, C. W., Cho, M. K., Won, D. H., Kim, C., Oh, H., Min, B. K. & Hwang, Y. J. electrochemical fragmentation of Cu<sub>2</sub>O nanoparticles enhancing selective C–C coupling from CO<sub>2</sub> reduction reaction. *J. Am. Chem. Soc.* **141**, 4624–4633 (2019).
33. Yuan, J., Zhi, W. Y., Liu, L., Yang, M. P., Wang, H. & Lu, J. X. Electrochemical reduction of CO<sub>2</sub> at metal-free N-functionalized graphene oxide electrodes. *Electrochim. Acta* **282**, 694–701 (2018).
34. Lai, Q. X., Zheng, L., Liang, Y. Y., He, J. P., Zhao, J. X. & Chen, J. H. Metal-organic-framework-derived Fe-N/C electrocatalyst with five-coordinated Fe-Nx sites for advanced oxygen reduction in acid media. *ACS Catal.* **7**, 1655–1663 (2017).
35. Lei, C. J., Wang, Y., Hou, Y., Liu, P., Yang, J., Zhang, T., Zhuang, X. D., Chen, M. W., Yang, B., Lei, L. C., Yuan, C., Qiu, M. & Feng, X. L. Efficient alkaline hydrogen evolution on atomically dispersed Ni-Nx Species anchored porous carbon with embedded Ni nanoparticles by accelerating water dissociation kinetics. *Energy Environ. Sci.* **12**, 149–156 (2019).
36. Hou, Y., Wen, Z. H., Cui, S. M., Ci, S. Q., Mao, S. & Chen, J. H. An advanced nitrogen-doped graphene/cobalt-embedded porous carbon polyhedron hybrid for efficient catalysis of oxygen reduction and water splitting. *Adv. Funct. Mater.* **25**, 872–882 (2015).
37. Xu, H., Cheng, D., Cao, D. & Zeng, X. C. A universal principle for a rational design of single-atom electrocatalysts. *Nat. Catal.* **1**, 339–348 (2018).
38. Nie, X., Luo, W., Janik, M. J. & Asthagiri, A. Reaction mechanisms of CO<sub>2</sub> electrochemical reduction on Cu(111) determined with density functional theory. *J. Catal.* **312**, 108–122 (2014).
39. Karamad, M., Hansen, H. A., Rossmeisl, J. & Nørskov, J. K. Mechanistic pathway in the electrochemical reduction of CO<sub>2</sub> on RuO<sub>2</sub>. *ACS Catal.* **5**, 4075–4081 (2015).
40. Peterson, A. A. & Nørskov, J. K. Activity descriptors for CO<sub>2</sub> electroreduction to methane on transition-metal catalysts. *J. Phys. Chem. Lett.* **3**, 251–258 (2012).
41. Nie, X., Esopi, M. R., Janik, M. J. & Asthagiri, A. Selectivity of CO<sub>2</sub> reduction on copper electrodes: the role of the kinetics of elementary steps. *Angew. Chem.* **52**, 2459–2462 (2013).
42. Xiao, H., Cheng, T., Goddard, W. A. & Sundararaman, R. Mechanistic explanation of the pH dependence and onset potentials for hydrocarbon products from electrochemical reduction of CO on Cu (111). *J. Am. Chem. Soc.* **138**, 483–486 (2016).
43. Kresse, G. & Furthmüller, J. Efficiency of ab-initio total energy calculations for metals and semiconductors using a plane-wave basis set. *Comput. Mater. Sci.* **6**, 15–50 (1996).
44. Kresse, G. & Hafner, J. Ab initio molecular dynamics for liquid metals. *Phys. Rev. B* **47**, 558–561 (1993).
45. Perdew, J. P., Burke, K. & Ernzerhof, M. Generalized gradient approximation made simple. *Phys. Rev. Lett.* **77**, 3865–3868 (1996).
46. Blöchl, P. E. Projector augmented-wave method. *Phys. Rev. B* **50**, 17953–17979 (1994).
47. Nørskov, J. K., Rossmeisl, J., Logadottir, A., Lindqvist, L., Kitchin, J. R., Bligaard, T. & Jónsson, H. Origin of the overpotential for oxygen reduction at a fuel-cell cathode. *J. Phys. Chem. B* **108**, 17886–17892 (2004).
48. Peterson, A. A., Abild-Pedersen, F., Studt, F., Rossmeisl, J. & Nørskov, J. K. How copper catalyzes the electroreduction of carbon dioxide into hydrocarbon fuels. *Energy Environ. Sci.* **3**, 1311–1315 (2010).

## Acknowledgements

This work was supported by National Natural Science Foundation of China (grant no. 21590813), Liaoning Revitalization Talents Program (grant no. XLYC1801003), the Fundamental Research Funds for the Central Universities (grant nos. DUT2019TA05 and DUT18LK20), and the Programme of Introducing Talents of Discipline to Universities (grant no. B13012). The computational work was supported by the National Key Research and Development Program of China (grant no. 2016YFB0600902). We acknowledge the Supercomputing Center of Dalian University of Technology and National SuperComputer Center in Tianjin for providing the computational resources for this work.

## Author contributions

K.Z. and X.N. contributed equally to this work. K.Z. and X.Q. conceived the idea and designed the experiments. K.Z. synthesized the catalysts. K.Z., S.C., and H.Y. performed the catalytic performance evaluations. X.N. and H.W. conducted the DFT calculations. K.Z., X.N., and J.G.C. analyzed the data. W.C., G.Z., and B.K. performed the EXAFS test. K.Z., X.N., X.Q., and J.G.C. co-wrote the paper. X.Q. and J.G.C. supervised the whole project.

## Competing interests

The authors declare no competing interests.

## Additional information


**Supplementary information** is available for this paper at <https://doi.org/10.1038/s41467-020-16381-8>.

**Correspondence** and requests for materials should be addressed to X.Q. or J.G.C.

**Peer review information** *Nature Communications* thanks the anonymous reviewers for their contributions to the peer review of this work. Peer review reports are available.

**Reprints and permission information** is available at <http://www.nature.com/reprints>

**Publisher's note** Springer Nature remains neutral with regard to jurisdictional claims in published maps and institutional affiliations.

 **Open Access** This article is licensed under a Creative Commons Attribution 4.0 International License, which permits use, sharing, adaptation, distribution and reproduction in any medium or format, as long as you give appropriate credit to the original author(s) and the source, provide a link to the Creative Commons license, and indicate if changes were made. The images or other third party material in this article are included in the article's Creative Commons license, unless indicated otherwise in a credit line to the material. If material is not included in the article's Creative Commons license and your intended use is not permitted by statutory regulation or exceeds the permitted use, you will need to obtain permission directly from the copyright holder. To view a copy of this license, visit <http://creativecommons.org/licenses/by/4.0/>.

© The Author(s) 2020